nature materials

LETTERS

PUBLISHED ONLINE: 17 FEBRUARY 2013 | DOI: 10.1038/NMAT3564

Enhanced tunnelling electroresistance effect due to a ferroelectrically induced phase transition at a magnetic complex oxide interface

Y. W. Yin[1,2], J. D. Burton[3], Y-M. Kim[4,5], A. Y. Borisevich[4], S. J. Pennycook[4], S. M. Yang[6], T. W. Noh[6], A. Gruverman[3], X. G. Li[2], E. Y. Tsymbal[3]* and Qi Li[1]*

The range of recently discovered phenomena in complex oxide heterostructures, made possible owing to advances in fabrication techniques, promise new functionalities and device concepts[1-3]. One issue that has received attention is the bistable electrical modulation of conductivity in ferroelectric tunnel junctions[4-6] (FTJs) in response to a ferroelectric polarization of the tunnelling barrier, a phenomenon known as the tunnelling electroresistance (TER) effect[7-10]. Ferroelectric tunnel junctions with ferromagnetic electrodes allow ferroelectric control of the tunnelling spin polarization through the magnetoelectric coupling at the ferromagnet/ferroelectric interface[11-17]. Here we demonstrate a significant enhancement of TER due to a ferroelectrically induced phase transition at a magnetic complex oxide interface. Ferroelectric tunnel junctions consisting of $BaTiO_3$ tunnelling barriers and $La_{0.7}Sr_{0.3}MnO_3$ electrodes exhibit a TER enhanced by up to ∼10,000% by a nanometre-thick $La_{0.5}Ca_{0.5}MnO_3$ interlayer inserted at one of the interfaces. The observed phenomenon originates from the metal-to-insulator phase transition in $La_{0.5}Ca_{0.5}MnO_3$, driven by the modulation of carrier density through ferroelectric polarization switching. Electrical, ferroelectric and magnetoresistive measurements combined with first-principles calculations provide evidence for a magnetoelectric origin of the enhanced TER, and indicate the presence of defect-mediated conduction in the FTJs. The effect is robust and may serve as a viable route for electronic and spintronic applications.

In the past few years, FTJs have aroused considerable interest owing to the rich physics involved in controlling their properties and potential application in nanoelectronics and data storage[18]. The seminal idea of a FTJ was proposed in ref. 19, but observation of the effect was hindered owing to the limited range of fabrication techniques available at the time. Recently, the FTJ concept has experienced a revival driven by significant advances in thin-film deposition and characterization techniques, leading to the discovery that ferroelectric films can maintain a stable and switchable polarization at nanometre thicknesses[6]. Very large TER effects were observed on $BaTiO_3$ (refs 7,8,10) and $Pb_{1-x}Zr_xTiO_3$ (ref. 9) ferroelectric thin films using scanning probe techniques that allow direct correlation of the ferroelectric polarization orientation and tunnelling conductance. There have been several successful demonstrations of the TER effect in trilayer patterned junctions that are suitable for device applications[13–15,17]. These experimental findings unambiguously prove the FTJ working principle[7], supporting earlier theoretical predictions[4,5].

The functionality of FTJs can be extended by using ferromagnetic electrodes to create a so-called multiferroic tunnel junction[11] (MFTJ). These constitute a four-state resistance device associated with two opposite ferroelectric polarization directions of the barrier and two different magnetization alignments of the electrodes[12–17]. (Note another type of MFTJ with a multiferroic barrier has also been proposed[20].) In MFTJs the magnetoelectric response enables the interfacial magnetic structures to be manipulated by an electric field through switching of the ferroelectric polarization[21–23]. For example, in the doped manganites $La_{1-x}A_xMnO_3$ (A = Ca, Sr or Ba; ref. 24), the ordering of the Mn moments in $La_{1-x}A_xMnO_3$ near the interface with a ferroelectric material may be altered by the accumulation or depletion of charge in response to the polarization, as found from first-principles calculations[25] and observed in experiments[26,27]. Furthermore, it was predicted that this electrically induced magnetic reconstruction produces a giant TER effect in FTJs that incorporate such interfaces[28]. The effect occurs owing to the highly spin-polarized manganite layer near the interface acting as an electrically controlled atomic-scale spin valve in series with the ferroelectric tunnel barrier that creates a switch for the tunnelling conductance.

Motivated by these theoretical predictions, we have fabricated $La_{0.7}Sr_{0.3}MnO_3$(50 nm)/$BaTiO_3$(3 nm)/$La_{0.5}Ca_{0.5}MnO_3$ (0.4–2 nm)/$La_{0.7}Sr_{0.3}MnO_3$(30 nm) planar tunnel junctions where the thin $La_{0.5}Ca_{0.5}MnO_3$ interlayer next to the ferroelectric $BaTiO_3$ barrier (Fig. 1a) provides the magnetoelectrically active response. In the remainder of this work we refer to these junctions as J1-*n* series, where *n* denotes the $La_{0.5}Ca_{0.5}MnO_3$ layer thickness in unit cells (u.c., 0.4 nm). For comparison, FTJs without the additional $La_{0.5}Ca_{0.5}MnO_3$ interface layer (referred to as J2), fabricated under the same conditions, were also studied[15]. The FTJs were grown epitaxially on $SrTiO_3$(001) substrates by pulsed-laser deposition (see Methods). Structural and chemical characterization of duplicate heterostructures fabricated under identical conditions were performed using scanning transmission electron microscopy

[1]Department of Physics, Pennsylvania State University, University Park, Pennsylvania 16802, USA, [2]Hefei National Laboratory for Physical Sciences at Microscale, Department of Physics, University of Science and Technology of China, Hefei 230026, China, [3]Department of Physics and Astronomy and Nebraska Center for Materials and Nanoscience, University of Nebraska, Lincoln, Nebraska 68588-0299, USA, [4]Materials Science and Technology Division, Oak Ridge National Laboratory, Tennessee 37831, USA, [5]Korea Basic Science Institute, Daejeon 305-806, Korea, [6]IBS-Center for Functional Interfaces of Correlated Electron Systems, Department of Physics and Astronomy, Seoul National University, Seoul 151-747, Korea.
*e-mail: tsymbal@unl.edu; qil1@psu.edu.

© 2013 Macmillan Publishers Limited. All rights reserved.

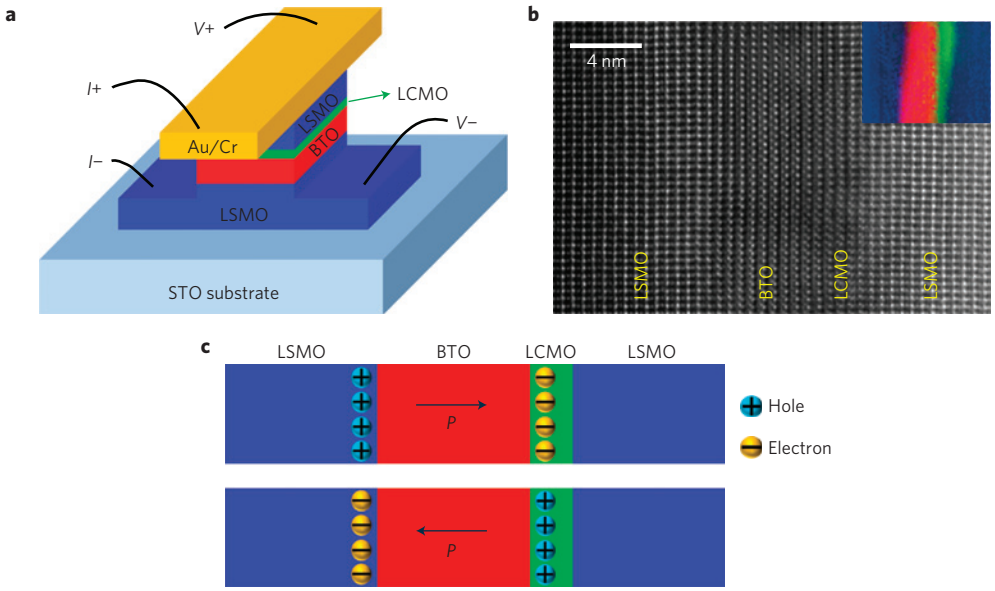

Figure 1 | Device geometry, atomic structure and polarization-induced charge accumulation in FTJs. a, A schematic diagram of the FTJ device geometry. **b**, The cross-sectional ADF STEM image at the interface region of an as-grown $La_{0.7}Sr_{0.3}MnO_3$(LSMO)/$BaTiO_3$(BTO)/$La_{0.5}Ca_{0.5}MnO_3$(LCMO)/$La_{0.7}Sr_{0.3}MnO_3$ tunnel junction (sample J1-2). The inset is the low-loss EELS map representing spectroscopic signatures of LSMO (blue), BTO (red) and LCMO (green). **c**, Schematic demonstration of the screening charge accumulation in electrodes for opposite ferroelectric polarization orientations in the BTO layer.

(STEM) with aberration correction and low-loss electron energy-loss spectroscopy[29] (EELS; see Methods). Annular dark-field (ADF) STEM imaging (Fig. 1b) of the interface region of an as-grown multilayer reveals a continuous barrier layer, and low-loss EELS mapping (Fig. 1b, inset) confirms the presence, position and expected thickness of the continuous $La_{0.5}Ca_{0.5}MnO_3$ layer (see Supplementary Fig. S1 and Supplementary Information for details). Our ADF data show enhancement of the c-constant in the $BaTiO_3$ region of the junction (Supplementary Fig. S2) with an average value of $c = 4.09 \pm 0.02$ Å, indicating a sizable tetragonal distortion of the ferroelectric layer, $c/a = 1.047 \pm 0.005$.

With the structures described above, we can now outline our expectations for their behaviour. The $La_{0.5}Ca_{0.5}MnO_3$ layer is chosen specifically at the doping boundary between the ferromagnetic–metallic phase ($x < 0.5$) and the antiferromagnetic–insulating phase ($x > 0.5$; ref. 30). For ferroelectric polarization pointing towards the thin $La_{0.5}Ca_{0.5}MnO_3$ layer (Fig. 1c, top panel), the electron accumulation or hole depletion induced to screen the polarization is expected to push the doping level of $La_{0.5}Ca_{0.5}MnO_3$ towards the $x < 0.5$ ferromagnetic–metallic phase. At the other interface of the $BaTiO_3$ barrier, the $La_{0.7}Sr_{0.3}MnO_3$ has stoichiometry that is far enough from the phase boundary and a change in magnetic order is not expected owing to a build-up of screening charge[25]. On the other hand, for polarization pointing away from the $La_{0.5}Ca_{0.5}MnO_3$ layer (Fig. 1c, bottom panel), the hole accumulation biases the interface towards the $x > 0.5$ side of the phase boundary, that is, towards the antiferromagnetic insulating phase. Such a magnetoelectrically induced metal–insulator transition in the $La_{0.5}Ca_{0.5}MnO_3$ would effectively increase the tunnelling barrier thickness, thereby leading to an exponential enhancement of the junction resistance, and hence to an overall TER effect.

As follows from our measurements and first-principles calculations described below, the FTJs exhibit these expected qualitative features. Figure 2a shows the resistance loops as a function of the pulsed poling voltage, V_{pulse}, at 40 K for a $15 \times 15\,\mu m^2$ area junction J1-2. Each data point in the hysteresis curve is tested at a fixed bias voltage of 10 mV after applying the corresponding 20 ms switching voltage pulse, V_{pulse}. The junction is in a high-resistance state when large enough positive V_{pulse} is applied to polarize the $BaTiO_3$ downward, and switches to a low-resistance state when ferroelectric polarization is reversed by large enough negative V_{pulse}. To quantify the resistance change we define the TER ratio,

$$\mathrm{TER} = \frac{R_{\downarrow} - R_{\uparrow}}{\min(R_{\uparrow}, R_{\downarrow})} \times 100\% \qquad (1)$$

in terms of the resistance of the up ($R_{\uparrow}$) and down ($R_{\downarrow}$) polarization states. From the data in Fig. 2a we find that it reaches up to 5,000% at 40 K, which is significantly larger than the TER values reported previously for planar FTJs (~10–100%; refs 13,14,17).

Junction J2 ($12 \times 12\,\mu m^2$), prepared under identical conditions as J1, but without an interfacial $La_{0.5}Ca_{0.5}MnO_3$ interlayer, also exhibits the R–V_{pulse} hysteresis loop at 40 K as shown in Fig. 2b. The TER ratio in this case, however, is only 30%, that is, two orders of magnitude smaller than that found for junction J1 under identical conditions. This fact clearly indicates the decisive role of the $La_{0.5}Ca_{0.5}MnO_3$ interlayer on the TER magnitude.

The TER effect becomes even larger at lower bias voltages and lower temperatures. Figure 2c shows current–voltage (I–V) characteristics for junction J1-2 at 5 K for both polarization states. The resulting TER ratio as a function of voltage is shown in the top inset of Fig. 2c. The TER ratio increases with decreasing bias and reaches up to ~10,000% at low biases. The TER ratio of junction J2 as a function of voltage is plotted in the bottom inset of Fig. 2c for comparison. It also increases with decreasing bias voltage, but is overall much smaller than for junction J1, peaking at ~45%.

The observed TER effect is reproducible and stable over many cycles. Figure 2d shows the resistance at 5 K for junction J1 subject to a series of consecutive reversals of the barrier polarization by voltage pulses ($V_{pulse} = \pm 1.4$ V, $t = 20$ ms). The resistance switches back and forth between two states repeatedly, with an average TER ~ 8,000% and no indication of deterioration. TER values obtained from such resistance switching measurements at different biases are plotted as stars in the top inset of Fig. 2c, and are consistent with TER values found directly from the full

© 2013 Macmillan Publishers Limited. All rights reserved.

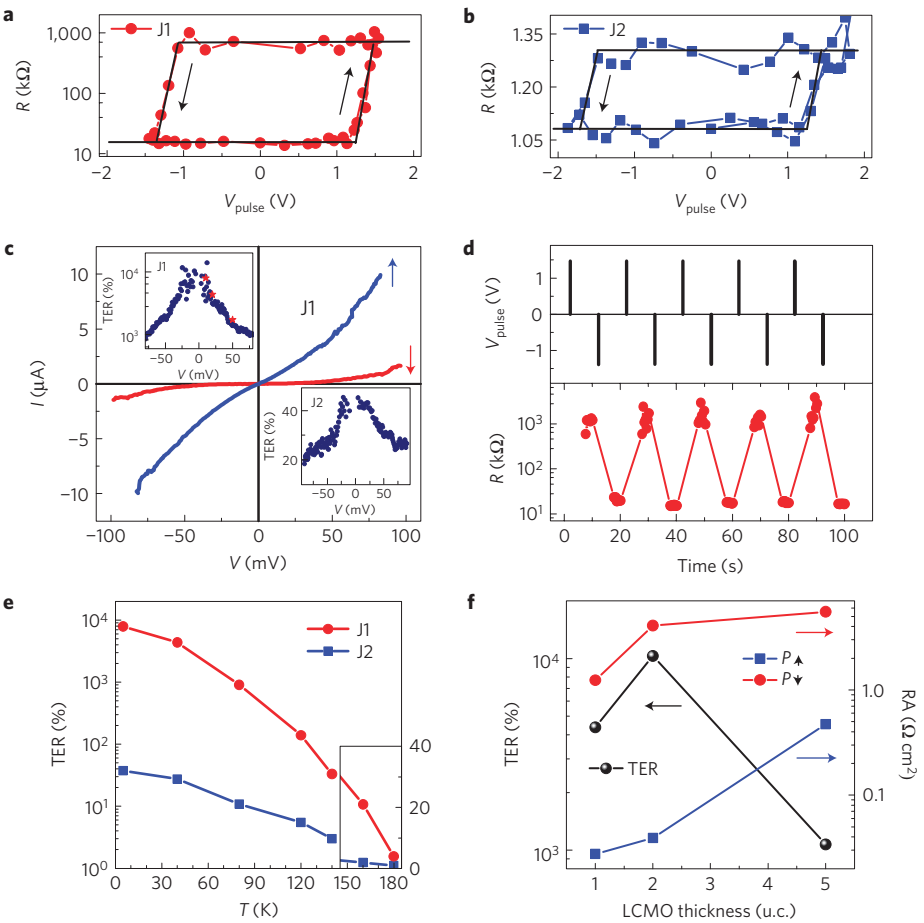

Figure 2 | Transport properties of FTJs. a,**b**, The resistance memory loops as a function of pulsed poling voltage (V_{pulse}) at 40 K for junctions J1-2 (**a**) and J2 (**b**). The solid lines are a guide to the eyes. The arrows indicate the direction of pulse sequence. **c**, Current–voltage curves of J1-2 at 5 K after the ferroelectric polarization was poled upward (blue) and downward (red). The arrows indicate ferroelectric polarization orientation. Top inset: bias dependence of TER ratios for J1-2 obtained from the *I*–*V* curves (round dots) and from the resistance switching measurements (star dots); bottom inset: bias dependence of TER ratios for J2 obtained from the *I*–*V* curves. **d**, Applied voltage pulse train (top panel) and the corresponding resistance switching (bottom panel) between upward- and downward-polarization states for J1-2 at 5 K and 10 mV. **e**, Temperature dependence of TER of junctions J1-2 and J2 measured at 10 mV. The inset uses a linear scale on the vertical axis to show the quenching of TER (<5%) at 180 K. **f**, TER and resistance area product (RA) for two polarization orientations ($P_{\uparrow}$ and $P_{\downarrow}$) for junctions J1−*n* as a function of $La_{0.5}Ca_{0.5}MnO_3$ layer thickness, *n*, at low temperatures.

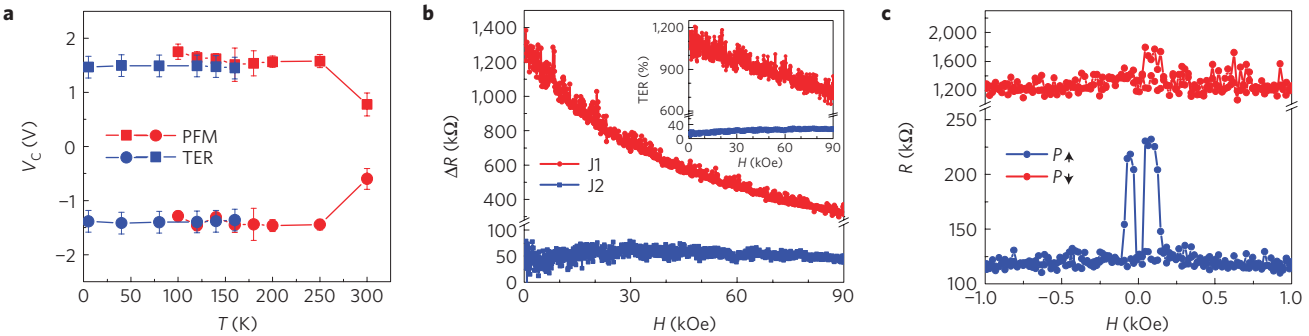

Figure 3 | Ferroelectric and magnetoresistive properties of FTJs. a, The coercive voltage (V_c) as a function of temperature determined from PFM amplitude (red symbols) and the threshold switching voltage obtained from TER measurements (blue symbols). Circles and squares indicate switching at negative and positive V_c, respectively. **b**, Resistance change, $\Delta R = R_{\downarrow} - R_{\uparrow}$, with polarization reversal as a function of applied magnetic field *H* for junctions J1-1 and J2 measured at $V = 10$ mV and $T = 80$ K. The inset shows corresponding TER ratios for the two junctions. **c**, Resistance (*R*) as a function of magnetic field (*H*) for junction J1-1 with the $La_{0.5}Ca_{0.5}MnO_3$ interlayer in the high- (top) and low- (bottom) resistance states.

I–*V* characteristics. Similar switching measurements have been performed several hundred times at different temperatures and biases, and a large reproducible TER has been observed in all cases, indicating a very robust effect.

The fact that the resistive switching is associated with ferroelectric polarization follows from our piezoresponse force microscopy (PFM) measurements (see Methods). The PFM results demonstrate a standard hysteretic electromechanical

© 2013 Macmillan Publishers Limited. All rights reserved.

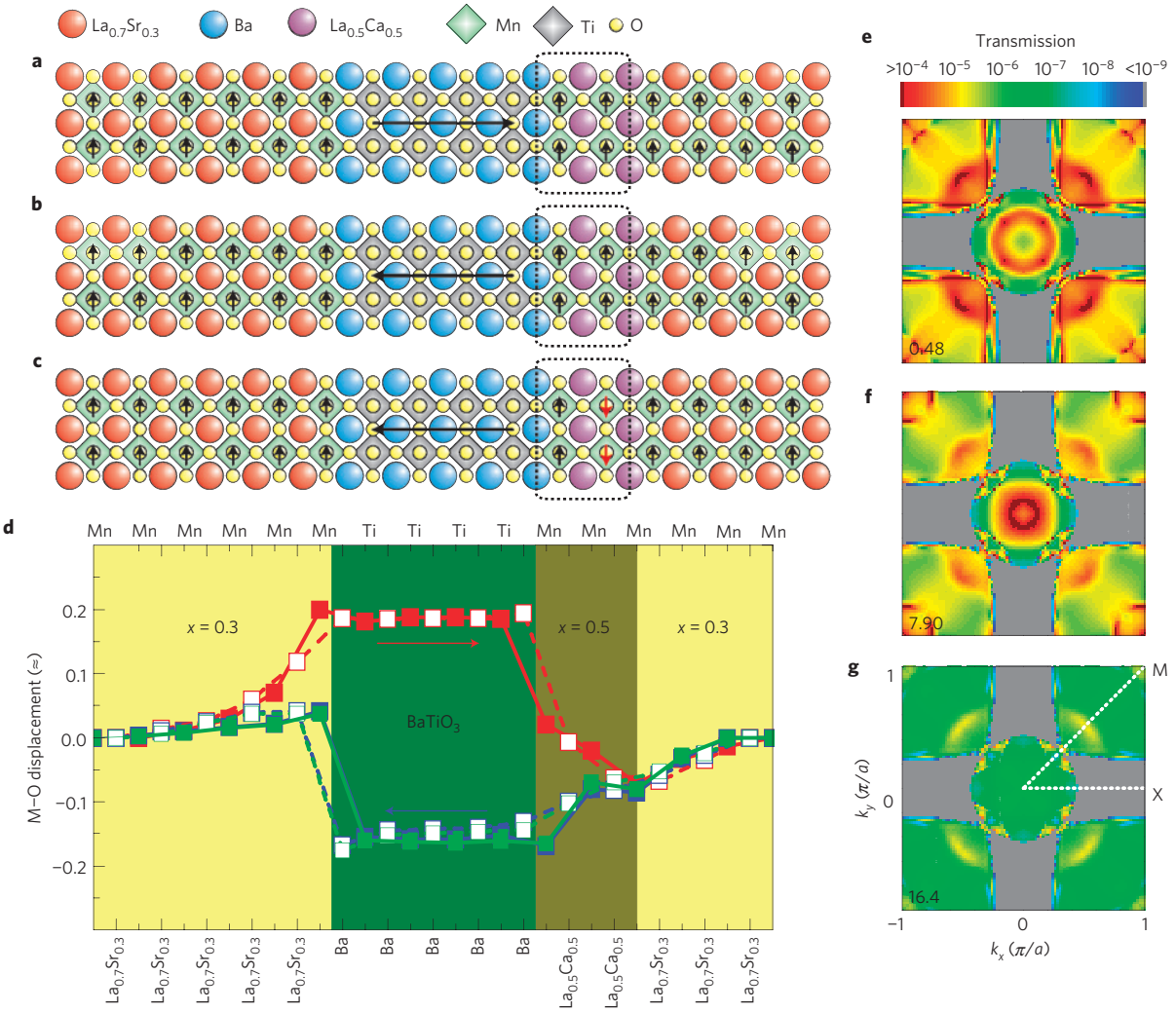

Figure 4 | Results of density functional calculations. a–c, Schematic side view of the layer-by-layer atomic positions and magnetoelectric state of the system. The ferroelectric polarization in the $BaTiO_3$ is indicated by large arrows, the magnetic moment on the Mn sites is indicated by the small arrows and the magnetoelectrically active region is indicated by the dashed rectangle on the right-hand interface. **a**, For polarization to the right, the Mn magnetic moments are ferromagnetically ordered throughout the right electrode. **b**, Configuration with polarization to the left where Mn magnetic moments are assumed to be ferromagnetically ordered everywhere. **c**, The ground-state magnetic configuration for polarization to the left. **d**, Profile of the relative metal–oxygen (M–O) displacements in each atomic layer for two polarization states. The filled symbols are B–O_2 displacements (B = Mn or Ti) and the open symbols are A–O displacements (A = $La_{0.7}Sr_{0.3}$, $La_{0.5}Ca_{0.5}$ or Ba). Red, blue and green symbols correspond to the magnetoelectric states depicted in **a–c**, respectively. **e–g**, The $\mathbf{k}_{\parallel}$-resolved distribution of the tunnelling transmission in the two-dimensional Brillouin zone for the different magnetoelectric states depicted in **a–c**, respectively. The integrated total conductance G per in-plane cell (see Methods) is given in the lower-left corner of each plot (in units of $10^{-6}e^2/h$). Note that the colour scale is logarithmic and the grey areas correspond to zero transmission.

response (Supplementary Figs S3 and S4), indicating a switchable ferroelectric polarization of the $BaTiO_3$ layer. Although with increasing temperature the polarization decreases, it remains non-zero up to room temperature. Figure 3a shows that the coercive voltage V_c for polarization reversal determined from the PFM hysteresis loops is weakly dependent on temperature (but reduced at $T = 300$ K). The coercive voltages (both positive and negative) are consistent with the threshold switching voltages obtained from TER data in a wide range of temperatures, indicating that the ferroelectric polarization reversal is the underlying mechanism for the resistive switching of our junctions.

Figure 2e shows the temperature dependence of TER for both J1-2 and J2 junctions. It is seen that TER decreases with temperature and becomes small (a few per cent) above ~180 K. This behaviour originates from defect-mediated inelastic tunnelling enabled at temperatures ~200 K, where conduction occurs through chains of localized states in the barrier[31], as discussed in the Supplementary Information. At these temperatures we observe a significant enhancement in conductance (Supplementary Fig. S5). The drop in TER follows from the high-resistance state exhibiting a stronger increase in conductance with temperature, owing to thermally activated inelastic tunnelling being less sensitive to polarization orientation. In addition, the enhanced conductance prevents poling the polarization state at a given voltage. As the result, when measuring resistance switching at elevated temperatures, the saturated ferroelectric state cannot be achieved. In addition, a decrease in the polarization amplitude (Supplementary Fig. S3) contributes to the drop of TER with increasing temperature.

The defect-mediated inelastic tunnelling is responsible for the strong reduction of TER with applied voltage (Fig. 3b, insets). The increasing bias voltage broadens the range of energies available for conduction, thus involving more resonant states in transport. The scale ~20 meV at which the TER drops is consistent with the

© 2013 Macmillan Publishers Limited. All rights reserved.

thermal energy associated with $T \sim 200$ K at which the onset of inelastic tunnelling occurs.

The magnetoelectric origin of the observed TER effect is supported by our magnetoresistance data. Figure 2g shows the resistance change, $\Delta R = R_{\downarrow} - R_{\uparrow}$, associated with ferroelectric polarization reversal as a function of applied magnetic field H. It is seen that the magnetic field markedly reduces ΔR for junction J1-1. This behaviour originates from alignment of $La_{0.5}Ca_{0.5}MnO_3$ magnetic moments altering the interfacial layer from insulating to metallic when polarization is pointing up. On the contrary, ΔR remains nearly unchanged for junction J2 where no $La_{0.5}Ca_{0.5}MnO_3$ layer is present. Furthermore, we find that tunnelling magnetoresistance (TMR) values are much larger for junctions J1-1 in a low resistance state than in a high resistance state. As seen from Fig. 3c, TMR is about 100% (at $T = 80$ K) in the low-resistance state, whereas TMR is hardly seen within the noise level for the same junction in the high resistance state. The significantly diminished TMR in the high-resistance state is consistent with the $La_{0.5}Ca_{0.5}MnO_3$ phase transition to the antiferromagnetic insulating state.

The TER effect is reproducible and has been observed in a variety of junctions with different $La_{0.5}Ca_{0.5}MnO_3$ interlayer thicknesses and different areas (see, for example, Supplementary Figs S6 and S7). As seen from Fig. 2f, the junction resistance increases with increasing $La_{0.5}Ca_{0.5}MnO_3$ thickness from 1 u.c. to 5 u.c. Samples with the $La_{0.5}Ca_{0.5}MnO_3$ interlayer of nominal 1 u.c. and 2 u.c. thickness systematically show larger TER than samples with thicker $La_{0.5}Ca_{0.5}MnO_3$. They all exhibit much larger TER ratios (>1,000%) than J2-type samples with no $La_{0.5}Ca_{0.5}MnO_3$ interlayer.

A third series of FTJs (labelled J3) was fabricated under identical conditions with the $La_{0.5}Ca_{0.5}MnO_3$ layer at the bottom interface, rather than at the top interface as in J1. As expected, the magnetoelectrically induced TER effect is much larger than for J2, but the TER ratio, as defined in equation (1), is negative and reaches about −500% at 5 K and low bias (Supplementary Fig. S8). The change in sign of TER is consistent with the reversal of the roles of up and down polarization as compared with J1. In J3 the upward polarization state corresponds to hole accumulation in the $La_{0.5}Ca_{0.5}MnO_3$, whereas the downward-polarization state corresponds to electron accumulation in the $La_{0.5}Ca_{0.5}MnO_3$. The reduced TER magnitude in J3 as compared with J1 can probably be traced back to the inherent asymmetry in interface structures produced during growth, as discussed in the Supplementary Information.

The enhancement of TER in FTJs with the $La_{0.5}Ca_{0.5}MnO_3$ interface layer is consistent with our first-principles density functional theory calculations (see Methods for details). The FTJ structure used in the calculations is shown schematically in Fig. 4a–c, with arrows distinguishing three different magnetoelectric states: polarization to the right, with Mn moments everywhere ferromagnetically ordered; polarization to the left with Mn moments everywhere forced to be ferromagnetically ordered; polarization to the left with antiferromagnetically ordered $La_{0.5}Ca_{0.5}MnO_3$. States with other magnetic configurations were also explored, but the three shown in Fig. 4a–c are the most relevant.

The calculated layer-by-layer cation–anion displacements are plotted in Fig. 4d for the three magnetoelectric configurations. Each state exhibits a nearly uniform polarization throughout the $BaTiO_3$ barrier virtually independent of the magnetic configuration. In all cases studied, polarization to the right was found to have lower energy than to the left, irrespective of the magnetic configuration. For polarization to the right, all tests of Mn magnetic moment reversal led to an increase in energy, indicating that ferromagnetic order throughout corresponds to the ground state. For polarization to the left, however, total energy calculations revealed that the state in Fig. 4c has the lowest energy (for example, 82 meV per interfacial Mn lower than the all-ferromagnetic state in Fig. 4b), indicating that polarization reversal indeed induces a significant magnetoelectric interface response, consistent with the previous calculations[25,28].

Calculations of the tunnelling conductance were performed as described in the Methods. Figure 3e–g shows the tunnelling transmission for all three structures as a function of the in-plane component of the Bloch wave vector, $\mathbf{k}_{\parallel}$, throughout the two-dimensional Brillouin zone. Comparing the two all-ferromagnetic states with different polarizations (Fig. 4e,f), we find a modest TER effect of ∼100%. This is analogous to what was found in our sample J2, where no magnetoelectrically induced phase change is expected, and therefore only a modest TER was observed. On the other hand, taking into account the induced change in magnetic order in the $La_{0.5}Ca_{0.5}MnO_3$ under polarization reversal we find a giant TER ratio of ∼3,300% (compare Figs 4e,g). These results are consistent with our experimental data and thus further confirm the magnetoelectric origin of the observed TER effect.

This mechanism of TER is conceptually different from those reported previously[6], such as the change in electrostatic potential through incomplete screening by the electrodes[4], effects related to ferroelectric ionic displacement at the interfaces[12], and the strain effect that changes the barrier width owing to the piezoelectric effect[5]. The ferroelectrically induced phase transition at the magnetic complex oxide interface in FTJs offers a new approach for bistable resistive devices with promising applications in nanoelectronics and data storage.

Methods

Fabrication and measurements. The oxide multilayers were epitaxially grown by pulsed laser deposition (KrF laser 248 nm) onto (001)-oriented $SrTiO_3$ substrates at a deposition temperature of 750 °C in a flowing oxygen atmosphere of 300 mtorr. After cooling down to room temperature, a Cr/Au bilayer was deposited immediately by d.c. magnetron sputtering on top of the multilayers for making electrical contacts in the later fabrication process. The deposition rate was pre-calibrated before film deposition with an accuracy of ∼20%. Thicknesses of $BaTiO_3$ and $La_{0.5}Ca_{0.5}MnO_3$ layers were confirmed by STEM measurements. The thicknesses quoted are all nominal values.

The junctions were fabricated into a cross-strip geometry using photolithography and Ar ion milling[15]. A SiO_2 layer was deposited using radiofrequency sputtering to create an insulating layer to allow the fabrication of the final gold contact leads to the top of the $La_{0.7}Sr_{0.3}MnO_3$ electrode. A schematic drawing of the FTJ structure is illustrated in Fig. 1a without showing the SiO_2 layer. The junction size tested was in the range from 5×5 to $70 \times 70\ \mu m^2$ and the data reported are for junction size less than $20 \times 20\ \mu m^2$.

Electrical and magneto-transport measurements were performed using a four-probe method in a Quantum Design PPMS system with a 9T superconducting magnet and a Janus cryostat with a 1 T electromagnet. Positive bias corresponds to current flow from the top to the bottom electrode. Both constant current and constant voltage biases have been used and when the constant voltage bias was used, an automatic feedback loop was turned on to ensure a constant voltage drop across the junction through the voltage leads. All resistances reported here are resistance values ($R = V/I$) recorded after the poling voltage pulse was removed. There is no measurable difference on the poling voltage duration tested between 20 ms and 1 s. The data reported here are for the poling voltage applied for 20 ms. All of the TER data shown are obtained for the parallel magnetization state of the two electrodes.

For the structural and chemical characterization at the atomic scale, a Nion UltraSTEM operating at 100 kV, equipped with a corrector of third- and fifth-order aberrations, and a Gatan Enfina spectrometer were used to obtain ADF STEM images and EELS spectrum images for samples. The convergence semi-angle for the electron probe was 31 mrad and the EELS collection semi-angle was 48 mrad. ADF signals for the samples were collected from the detector inner-angle of ∼86 mrad.

Piezoresponse force microscopy measurements were performed on junction J1-5. The temperature-dependent PFM amplitude and phase data were obtained using a JSPM-5410 (Jeol) scanning probe microscope under high vacuum (below 10–4 Pa). Temperature was varied from 100 to 300 K. An a.c. probing voltage ($f = 128$–130 kHz) with an amplitude of 1.0 V was applied using a diamond-coated conductive tip (CDT-CONTR, Nanosensors). A lock-in amplifier (Model 7265, Signal Recovery) was used to detect the piezoresponse signals. The frequency of the sweeping voltage used for measuring PFM loops was set equal to 5 Hz. Representative PFM amplitude and phase data are shown in Supplementary Figs S3 and S4, respectively, confirming the ferroelectric switching behaviour of the junction up to room temperature.

© 2013 Macmillan Publishers Limited. All rights reserved.

Calculations. Density functional calculations were performed using the plane-wave pseudopotential method implemented in Quantum-ESPRESSO (ref. 32). The periodic supercell used in the calculations consists of 8 u.c. of $La_{0.7}Sr_{0.3}MnO_3$, 4.5 u.c. of $BaTiO_3$, 2 u.c. of $La_{0.5}Ca_{0.5}MnO_3$ at one interface with $BaTiO_3$, plus one additional MnO_2 monolayer at the boundary between the $x = 0.3$ and 0.5 layers. We treat the La–Sr and La–Ca substitutional doping in a generic way, known as the virtual crystal approximation, by modelling each perovskite A-site cation with a pseudopotential with fractional valence. Exchange and correlation are treated using the generalized gradient approximation. All calculations use an energy cutoff of 400 eV for the plane wave expansion. Atomic relaxations of the supercell are performed using a $6 \times 6 \times 1$Monkhorst–Pack grid for k-point sampling and atomic positions are converged until the Hellmann–Feynman forces on each atom became less than 20 meV $Å^{-1}$. The in-plane lattice constant of the supercell is constrained to the calculated value for bulk cubic $SrTiO_3$, $a = 3.937$ Å. The two polarization states of $BaTiO_3$ are obtained by relaxing the atomic structure under the initial condition of either positive or negative z-displacements of the Ti ions with respect to their neighbouring O anions. Subsequent self-consistent calculations of the supercell using a dense $20 \times 20 \times 1$ k-point grid are performed to determine total energies of the different magnetoelectric configurations, similar to the previous works[25,28].

The transport properties were calculated using a general scattering formalism implemented in Quantum-ESPRESSO (ref. 32). The supercell described above is considered as the scattering region, ideally attached on both sides to semi-infinite $La_{0.7}Sr_{0.3}MnO_3$ leads. We assume perfect periodicity in the plane parallel to the interfaces so that the in-plane component of the Bloch wave vector, $\mathbf{k}_\parallel$, is preserved for all single-electron states, including those that contribute to the tunnelling conductance. The two-dimensional Brillouin zone is sampled using a uniform 100×100 $\mathbf{k}_\parallel$ mesh. The conductance per unit cell area is related to the transmission by the Landauer–Büttiker formula,

$$G_\sigma = \frac{e^2}{h} \sum_{\mathbf{k}_\parallel} T_\sigma(\mathbf{k}_\parallel)$$

where $T_\sigma(\mathbf{k}_\parallel)$ is the transmission probability of an electron at the Fermi energy with spin σ and Bloch wave vector $\mathbf{k}_\parallel = (k_x, k_y)$.

Received 3 May 2012; accepted 7 January 2013; published online 17 February 2013

References

1. Mannhart, J. & Schlom, D. G. Oxide interfaces—An opportunity for electronics. *Science* **327,** 1607–1611 (2010).
2. Zubko, P., Gariglio, S., Gabay, M., Ghosez, P. & Triscone, J-M. Interface physics in complex oxide heterostructures. *Ann. Rev. Condens. Matter Phys.* **2,** 141–165 (2011).
3. Hwang, H. Y. *et al.* Emergent phenomena at oxide interfaces. *Nature Mater.* **11,** 103–113 (2012).
4. Zhuravlev, M. Y., Sabirianov, R. F., Jaswal, S. S. & Tsymbal, E. Y. Giant electroresistance in ferroelectric tunnel junctions. *Phys. Rev. Lett.* **94,** 246802 (2005).
5. Kohlstedt, H., Pertsev, N. A., Rodriguez Contreras, J. & Waser, R. Theoretical current–voltage characteristics of ferroelectric tunnel junctions. *Phys. Rev. B* **72,** 125341 (2005).
6. Tsymbal, E. Y. & Kohlstedt, H. Tunneling across a ferroelectric. *Science* **313,** 181–183 (2006).
7. Garcia, V. *et al.* Giant tunnel electroresistance for non-destructive readout of ferroelectric states. *Nature* **460,** 81–84 (2009).
8. Gruverman, A. *et al.* Tunneling electroresistance effect in ferroelectric tunnel junctions at the nanoscale. *Nano Lett.* **9,** 3539–3543 (2009).
9. Maksymovych, P. *et al.* Polarization control of electron tunneling into ferroelectric surfaces. *Science* **324,** 1421–1425 (2009).
10. Chanthbouala, A. *et al.* Solid-state memories based on ferroelectric tunnel junctions. *Nature Nanotech.* **7,** 101–104 (2012).
11. Zhuravlev, M. Y., Jaswal, S. S., Tsymbal, E. Y. & Sabirianov, R. F. Ferroelectric switch for spin injection. *Appl. Phys. Lett.* **87,** 222114 (2005).
12. Velev, J. P. *et al.* Magnetic tunnel junctions with ferroelectric barriers: prediction of four resistance states from first principles. *Nano Lett.* **9,** 427–432 (2009).
13. Garcia, V. *et al.* Ferroelectric control of spin polarization. *Science* **327,** 1106–1110 (2010).
14. Hambe, M. *et al.* Crossing an interface: Ferroelectric control of tunnel currents in magnetic complex oxide heterostructures. *Adv. Funct. Mater.* **20,** 2436–2441 (2010).
15. Yin, Y. W. *et al.* Coexistence of tunneling magnetoresistance and electroresistance at room temperature in $La_{0.7}Sr_{0.3}MnO_3/(Ba,Sr)TiO_3/La_{0.7}Sr_{0.3}MnO_3$ multiferroic tunnel junctions. *J. Appl. Phys.* **109,** 07D915 (2011).
16. Pantel, D., Goetze, S., Hesse, D. & Alexe, M. Reversible electrical switching of spin polarization in multiferroic tunnel junctions. *Nature Mater.* **11,** 289–293 (2012).
17. Yin, Y. W. *et al.* Multiferroic tunnel junctions. *Front. Phys.* **7,** 380–385 (2012).
18. Tsymbal, E. Y., Gruverman, A., Garcia, V., Bibes, M. & Barthélémy, A. Ferroelectric and multiferroic tunnel junctions. *Mater. Res. Soc. Bull.* **37,** 138–143 (2012).
19. Esaki, L., Laibowitz, R. B. & Stiles, P. J. Polar switch. *IBM Tech. Discl. Bull.* **13,** 2161 (1971).
20. Gajek, M. *et al.* Tunnel junctions with multiferroic barriers. *Nature Mater.* **6,** 296–302 (2007).
21. Duan, C-G., Jaswal, S. S. & Tsymbal, E. Y. Predicted magnetoelectric effect in $Fe/BaTiO_3$ multilayers: Ferroelectric control of magnetism. *Phys. Rev. Lett.* **97,** 047201 (2006).
22. Niranjan, M. K., Burton, J. D., Velev, J. P., Jaswal, S. S. & Tsymbal, E. Y. Magnetoelectric effect at the $SrRuO_3/BaTiO_3$ (001) interface: An *ab initio* study. *Appl. Phys. Lett.* **95,** 052501 (2009).
23. Valencia, S. *et al.* Interface-induced room-temperature multiferroicity in $BaTiO_3$. *Nature Mater.* **10,** 753–758 (2011).
24. Dagotto, E., Hotta, T. & Moreo, A. Colossal magnetoresistant materials: The key role of phase separation. *Phys. Rep.* **344,** 1–153 (2001).
25. Burton, J. D. & Tsymbal, E. Y. Prediction of electrically induced magnetic reconstruction at the manganite/ferroelectric interface. *Phys. Rev. B* **80,** 174406 (2009).
26. Molegraaf, H. J. A. *et al.* Magnetoelectric effects in complex oxides with competing ground states. *Adv. Mater.* **21,** 3470–3474 (2009).
27. Vaz, C. A. F. *et al.* Origin of the magnetoelectric coupling effect in $Pb(Zr_{0.2}Ti_{0.8})O_3/La_{0.8}Sr_{0.2}MnO_3$ multiferroic heterostructures. *Phys. Rev. Lett.* **104,** 127202 (2010).
28. Burton, J. D. & Tsymbal, E. Y. Giant tunneling electroresistance effect driven by an electrically controlled spin valve at a complex oxide interface. *Phys. Rev. Lett.* **106,** 157203 (2011).
29. Chang, H. J. *et al.* Atomically resolved mapping of polarization and electric fields across ferroelectric/oxide interfaces by Z-contrast imaging. *Adv. Mater.* **23,** 2474–2479 (2011).
30. Schiffer, P., Ramirez, A. P., Bao, W. & Cheong, S. W. Low temperature magnetoresistance and the magnetic phase diagram of $La_{1-x}Ca_xMnO_3$. *Phys. Rev. Lett.* **75,** 3336 (1995).
31. Glazman, L. I. & Matveev, K. A. Inelastic tunneling through thin amorphous films. *Sov. Phys. JETP* **67,** 1276–1282 (1988).
32. Giannozzi, P. *et al.* QUANTUM ESPRESSO: A modular and open-source software project for quantum simulations of materials. *J. Phys. Condens. Matter* **21,** 395502 (2009).

Acknowledgements

The work at Pennsylvania State University (PSU) was supported in part by the DOE (Grant No. DE-FG02-08ER4653) and the NSF (Grant No. DMR-1207474). The PSU NSF MRSEC seed grant and NNIN Nanofabrication facilities are acknowledged. The work at USTC was supported by NBRP-2012CB922003 and NSFC. The work at the University of Nebraska-Lincoln (UNL) was supported by NSF MRSEC (Grant No. DMR-0820521) and NSF EPSCoR (Grant No. EPS-1010674). Computations were performed at the UNL Holland Computing Center. The work at ORNL was supported by the Materials Science and Engineering Division of the US DOE.

Author contributions

E.Y.T. and J.D.B. predicted the magnetoelectrically induced TER effect and stimulated the experimental studies. Q.L. designed and supervised the experiment. Y.W.Y. fabricated samples and performed transport measurements. Q.L., Y.W.Y. and X.G.L. analysed the data. Y-M.K. and A.Y.B. carried out STEM and EELS measurements in the laboratory led by S.J.P. S.M.Y. performed PFM measurements under the supervision of T.W.N. A.G. assisted in analysing the PFM data. J.D.B. carried out theoretical calculations under the supervision of E.Y.T. Q.L., E.Y.T., Y.W.Y. and J.D.B. wrote the manuscript. All authors contributed to the refinement of the manuscript.

Additional information

Supplementary information is available in the online version of the paper. Reprints and permissions information is available online at www.nature.com/reprints. Correspondence and requests for materials should be addressed to E.Y.T. or Q.L.

Competing financial interests

The authors declare no competing financial interests.

© 2013 Macmillan Publishers Limited. All rights reserved.